

Magnetoresistance of vertical Co-graphene-NiFe junctions controlled by charge transfer and proximity-induced spin splitting in graphene

P. U. Asshoff¹, J. L. Sambricio¹, A. Mishchenko¹, A.P. Rooney², E.W. Hill³, S. J. Haigh²,
A. K. Geim¹, V. I. Fal'ko^{1,3}, I. J. Vera-Marun¹, I. V. Grigorieva¹

¹*School of Physics and Astronomy, University of Manchester, Oxford Road, Manchester M13 9PL, UK*

²*School of Materials, University of Manchester, Oxford Road, Manchester M13 9PL, UK*

³*National Graphene Institute, University of Manchester, Manchester M13 9PL, UK*

Graphene is hailed as potentially an ideal material for spintronics due to weak intrinsic spin-orbit interaction that facilitates spin transport, and tunability of its electronic properties [1-3]. Additional functionalities in graphene-based spintronic devices can be achieved by inducing magnetism in graphene [3-8]. A less explored potential of graphene is related to the role it can play in vertical magnetoresistive devices [9-16], the most prominent class of spintronic devices widely used as magnetic sensors. We report observations of magnetoresistance (MR) in vertical Co-graphene-NiFe junctions, where the number of graphene layers, N , is varied from 1 to 4. For all N graphene efficiently separates the ferromagnetic electrodes ensuring their independent switching but the sign of MR depends on N and is inverted at relatively small bias voltages. This anomalous behavior is consistent with proximity-induced exchange splitting in graphene in contact with a ferromagnet, so that the role of ferromagnetic electrodes in the junction is played by proximitised layers of graphene. We demonstrate that the sign of MR depends on the charge transfer between graphene and the adjacent ferromagnetic metal. Our results suggest a new architecture for vertical MR devices, with electrically controlled MR effect.

Theoretical proposals [9,10] for graphene-based vertical magnetoresistive junctions focused on the so-called 'K-point filtering' in ideally lattice-matched single-crystalline ferromagnet-graphene-ferromagnet (FM-G-FM) structures, where perfect spin filtering at FM-G interfaces is expected to arise from matching spin-polarized bands in the ferromagnet and the electronic states in graphene. This mechanism is believed to be responsible for the MR sign inversion observed in Ni-Al₂O₃-Co tunnel junctions where the Ni electrode was passivated by CVD grown (epitaxial) monolayer graphene [11-13]. However, despite several attempts, no significant spin filtering could so far be achieved in vertical magnetoresistive devices where graphene was used as a spacer between two FM electrodes [14-19], in contrast to theory predictions [9,10]. The most likely reason for this is that FM-G-FM sandwiches (especially those fabricated by a combination of graphene transfer and deposition of FM films) are in fact van der Waals heterostructures [20] rather than truly lattice-matched crystals. In this case, as we show below, graphene plays a different role, itself becoming a source of spin-polarized electrons due to the interplay of (i) its doping by charge transfer from the FM metal and (ii) proximity-induced exchange splitting in graphene that has been recently demonstrated in lateral spin-valve structures [6].

To explore such a possibility, one needs to create contamination- and oxidation-free G-FM interfaces, but without the requirement of lattice matching between G and the FMs. To this end, we have fabricated vertical FM-G-FM' devices where ultimately clean G-FM interfaces were obtained by depositing the ferromagnetic metals on the two sides of a suspended graphene membrane, thereby preventing oxidation, minimizing the number of fabrication steps and limiting the exposure of the devices to solvents during preparation (here FM=Co and FM'=Ni_{0.8}Fe_{0.2} alloy). Details of sample fabrication and characterization are given in Methods and Supplementary Figures S1-S3. Briefly, an exfoliated graphene (or hBN) flake was suspended over a 3-4 μm diameter circular aperture in a 100 nm-thick SiN_x membrane using a dry transfer method [21]. The FM electrodes were then evaporated onto the suspended flake from the top and bottom side as shown schematically in Fig. 1(a) and Supplementary Fig. S1 (a similar approach was used in ref. [14], but our method is different in several important aspects (Methods and Supplementary Note 1)). After the first (top) deposition, the metal at the interface was protected from oxidation by graphene, as the latter is known to act as an impermeable barrier for all gases and liquids [11,22].

As a test of our fabrication procedure, we first made a device where Co and Ni_{0.8}Fe_{0.2} (Py) electrodes were separated by bilayer hexagonal boron nitride (hBN) instead of graphene. Atomically thin hBN has been shown to act as a high-quality insulating barrier in vertical transistors [23], lateral spin valves [24] and, most recently, in magnetic tunnel junctions (MTJs) [25]. Figures 1b,c show magneto-transport characteristics of our FM-hBN-FM' device. These are

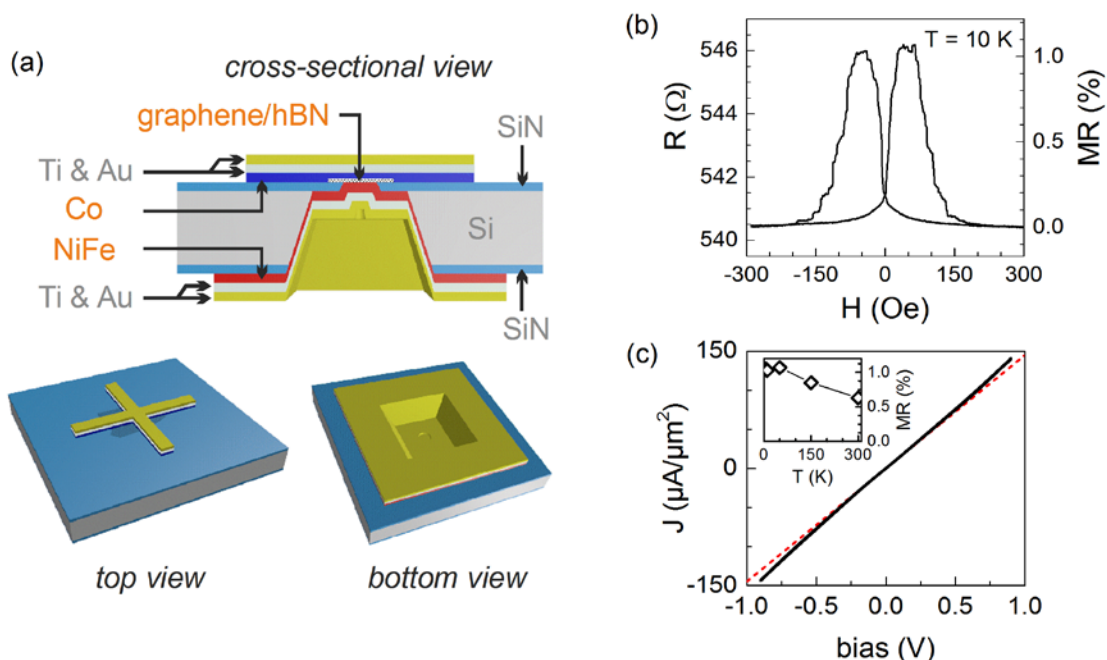


FIG. 1. Sample design and magnetoresistance of the reference hBN device. (a) Design of the sample. Ferromagnetic Co and Ni_{0.8}Fe_{0.2} films (each 20 nm thick) were deposited on the top and bottom side, respectively, of graphene (or hBN) suspended over an 3.5 μm diameter aperture in a 100 nm thick SiN_x window. On the top side, a Greek cross geometry was used. On the bottom side, a larger square area was covered by the NiFe/Ti/Au film. (b) Resistance R of the hBN-based device vs the applied magnetic field H ($T=10$ K); $\text{MR} \approx 1\%$. Shown behavior is typical for all T up to 300 K. (c) **Main panel:** Current-voltage characteristic of the hBN-based device at $T = 10$ K

(black solid line). Its tangent line at zero bias (red dashed line) is shown to illustrate a slight bending of the curve for higher bias, indicative of tunneling behavior. **Inset:** temperature dependence of the MR (\diamond). The line is a guide to the eye.

consistent with classical MTJ behavior: The two electrodes are magnetically separated and switch independently, with a TMR value of $\approx 1\%$ at a temperature $T = 10$ K. Using Jullière's formula [26] $TMR = 2P_1P_2/(1 - P_1P_2)$ and a simplifying assumption $P_1 = P_2 = P$ (equal spin polarization for both FM electrodes) we obtain an average spin polarization of the ferromagnets $P \sim 10\%$. These characteristics compare very favorably with $P \sim 0.05 - 0.25\%$ and TMR $\sim 0.3-0.5\%$ reported for Co/hBN/NiFe MTJs based on hBN grown by chemical vapor deposition (CVD) and transferred onto the FM [27] and are of the same order as the more recent work [25] where the hBN barrier in Fe/hBN/Co MTJs was grown directly on Fe. The temperature-dependent MR shown in the inset of Fig. 1(c) is also in agreement with the usual TMR behavior [26-29]: the MR decreases by 40% as the temperature is increased from 5 K to 300 K, which is commonly attributed to magnon excitations [28,29]. Furthermore, the non-linear $I(V)$ characteristics (Fig. 1c) and the resistance \times area product (RA) of $6.2 \text{ k}\Omega \cdot \mu\text{m}^2$ at 10 K agree with previous measurements on a 2-layer hBN tunnel barrier [30]. Finally, we have checked that our fabrication method does not lead to unintentional contacts between the top and bottom FM films by preparing several test samples without the graphene-covered aperture and found resistances $>10 \text{ M}\Omega$, confirming that the current flows through the junction area only.

Having proven the technology, we fabricated a set of ten Co-G-Py structures, where FM electrodes are separated by mono-, bi-, tri- or four-layer graphene, and studied their vertical magnetoresistance. The sample design is shown in Fig. 1(a). Typical variations of the MR as a function of in-plane magnetic field, H , at different temperatures, T , are shown in the top row of Fig. 2a and Supplementary Fig. S5. Similar to the hBN-based MTJ device, all graphene-based junctions showed positive MR, with plateau regions in the $R(H)$ traces indicating that already a monolayer of graphene is sufficient to decouple the switching of the two FMs, as expected in a MTJ device. At the same time, the resistance of all devices was quite low (between 2 and 20 Ω) and $I(V)$ characteristics were linear (Supplementary Fig. S4), corresponding to metallic behavior. This is in stark contrast to previous reports [14-16] where graphene-based structures showed tunneling behavior, presumably due to residual contamination. Concerning the origin of MR, we used angle-dependent measurements to verify that it was not due to anisotropic magnetoresistance.

In terms of RA and MR values, there was no correlation between the number of graphene layers, N , separating the FM electrodes and the device behavior (top row of Fig. 2a, Fig. 3a and Supplementary Fig. S5), despite the identical fabrication conditions. For example, for three $N=2$ devices the measured RA products were 17, 29 and 309 $\Omega \cdot \mu\text{m}^2$, with MR = 1.03%, 0.66% and 0.10%; for two $N=4$ devices these were 38 and 136 $\Omega \cdot \mu\text{m}^2$, or 0.42% and 0.12%, respectively. A similarly large spread of characteristics was found for $N=3$ (RA = 23, 170, 193 $\Omega \cdot \mu\text{m}^2$ with MR = 0.9%, 0.30%, 0.12%) and $N=1$ (RA = 110, 175 $\Omega \cdot \mu\text{m}^2$ with MR = 0.09%, 0.2%) junctions. The contribution from the resistance of gold leads, $\sim 1\Omega$, could only play a role for two devices with the smallest R (see above).

Furthermore, the large average value of RA across all samples, $120 \Omega \cdot \mu\text{m}^2$ (much higher than for a typical metal), the almost temperature-independent RA for most devices or RA increasing at low T , as seen for $N=3$ and 4 in Fig. 3a, are a strong indication that the measured R of the devices is determined by the resistance of G-FM interfaces and not the metallic leads [31].

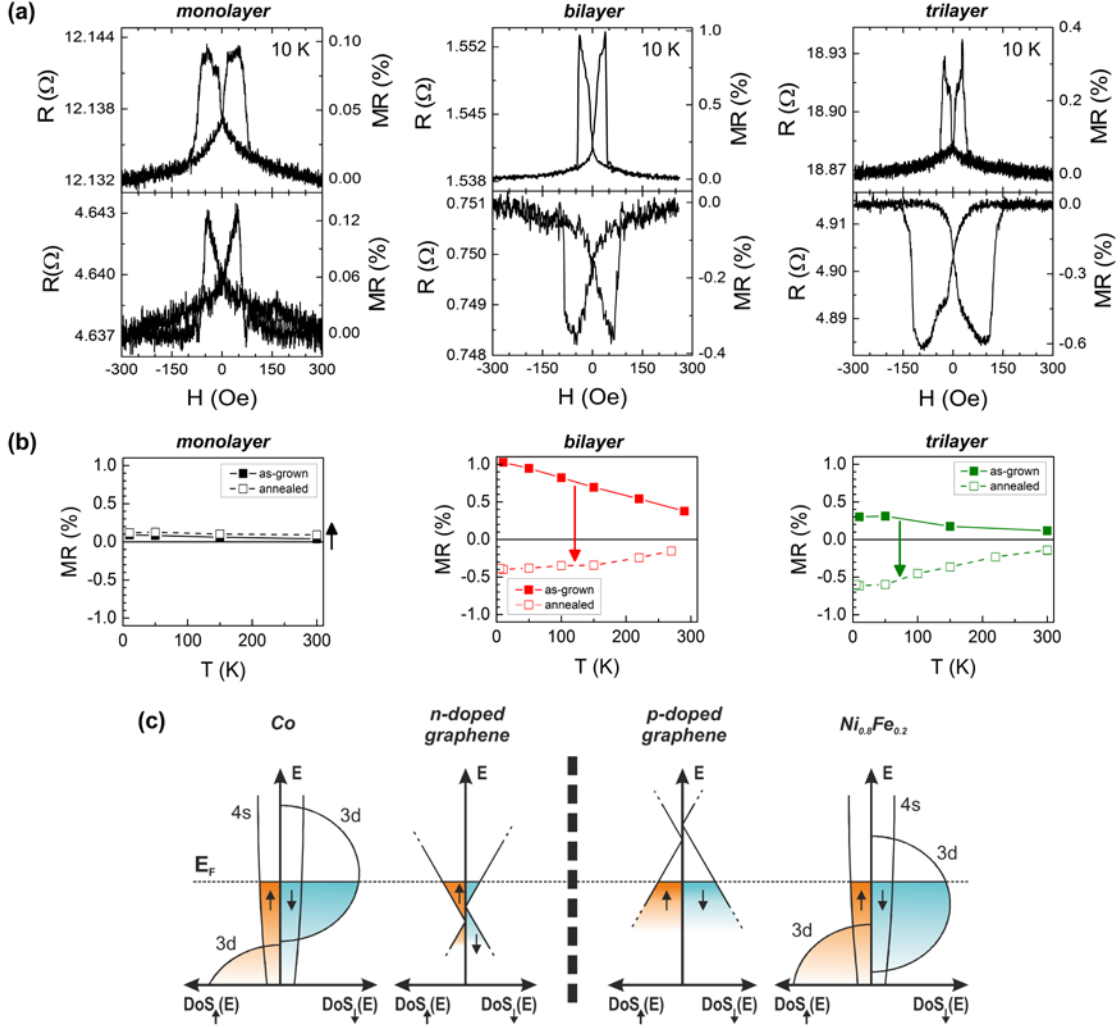


FIG. 2. Magnetoresistance of graphene-based vertical junctions as a function of the number of layers. (a) Low-temperature MR traces for mono-, bi- and trilayer graphene devices before and after annealing (top and bottom panels, respectively). For $N=2$ and 3, MR changes sign, which is accompanied by an increase in coercivity of the Co electrode. (b) Temperature-dependent MR of mono-, bi- and trilayer graphene devices before ($\square, \square, \square$) and after ($\blacksquare, \blacksquare, \blacksquare$) annealing. Arrows indicate the change in MR after annealing. (c) Schematic spin-dependent density of states, $\text{DoS}_{\uparrow/\downarrow}(E)$, for the constituent layers of a device with $N \geq 2$ (see text). The Fermi levels of graphene layers adjacent to the FMs are shifted due to n-doping and p-doping from Co and Py, respectively. Proximity-induced exchange splitting results in different DoSs for graphene's spin-up and spin-down carriers at E_F . The thick dashed line in the middle indicates separation of the van der Waals bonded graphene layers as they conform to the FM films (see text).

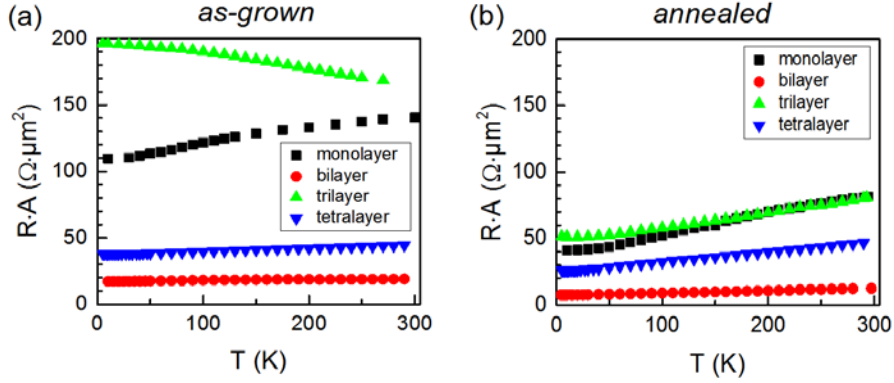


FIG. 3. Temperature dependence of the RA product before and after annealing. (a) Temperature dependences of the RA product for $N=1$ (■), $N=2$ (●), $N=3$ (▲) and $N=4$ (▼) graphene devices before annealing. No correlation can be discerned between N and the device resistance and neither of the samples shows a metal-like $RA(T)$ dependence. (b) Temperature dependences of the RA product for the same devices after annealing. All devices show metal-like behavior, with a significant reduction in RA values compared to their as-grown state.

The surprisingly wide spread of (magneto)transport characteristics of our devices and the apparent lack of dependence on N can be understood if we recall that the deposition of relatively thick, ~ 150 nm, metallic films on suspended, atomically thin graphene membranes results in significant strains in the devices, evident from their topography at different stages of preparation, e.g., the ‘Mexican hat’ shape shown in Supplementary Fig. S2. Strains will inevitably affect, locally, the atomic scale separation between the FM and the adjacent graphene layer. To relieve such strains and further improve the interface quality, we annealed several representative devices with different N at 300 °C in Ar/H₂ atmosphere for up to 10 h. Annealing under such conditions is known to significantly improve the interfaces in van der Waals heterostructures [21,32]. This resulted in a strong change in both RA and MR, leading to a consistent behavior of all devices – c.f. Figs. 3a and 3b. The RA of all samples dropped significantly after annealing, from $17 - 196 \Omega \cdot \mu\text{m}^2$ to $8 - 51 \Omega \cdot \mu\text{m}^2$ at 10 K, and its temperature dependence became metal-like for all devices, unlike the almost flat or slightly increasing RA at low T for the as-prepared samples. The change in magnetoresistance was even more dramatic: For devices with $N=2$ and 3 MR changed sign and in some cases increased in absolute value (e.g., for $N=3$ at $T=10\text{K}$ from $+0.30\%$ before annealing to -0.6% after), see Fig. 2a,b. For $N=4$ it dropped from $\text{MR} = 0.4\%$ to essentially zero (Supplementary Fig. S6). Only for the monolayer device, $N=1$, MR remained small and positive, slightly increasing from 0.1% to 0.14% .

Another change in device behavior becomes clear from comparison of the coercivities of the FM layers before and after annealing (Fig. 2a): these increased significantly, especially for $N=2$ and $N=3$, indicating more uniform magnetization in our polycrystalline FM films. It is therefore natural to attribute the increase in coercivity to relaxation of stresses both in the FMs and at the interface between a FM and the adjacent graphene layer. We note that the annealing temperature was too low to expect any significant recrystallization and, indeed, no noticeable

changes in grain sizes could be seen when the FM films were observed through transparent graphene in a scanning electron microscope (SEM), see Supplementary Fig. S3. Nevertheless, SEM observations of test samples (only one FM deposited on graphene, before and after annealing) did show signs of rearrangements of the individual crystallites in our polycrystalline FM films after annealing (Supplementary Fig. S3), which can be attributed to strain relaxation. The lower device resistances after annealing (see above) are also consistent with relaxation of strains at the interfaces, resulting in improved contact between FM and graphene due to better conformation of the adjacent graphene layers to the non-flat topography of the polycrystalline FM films [33].

Just an improved contact between graphene and FMs cannot account for the main feature in the behavior of our devices: the sign change of MR after annealing. The widely discussed ‘K-point spin filtering’, suggested by theory for both graphene-FM and hBN-FM epitaxial interfaces [9,10] and used to interpret a number of experimental findings [11,15,19], cannot explain the sign change of MR and, more importantly, is not applicable to our devices. Firstly, the polycrystalline nature of our FM films and the corresponding lack of epitaxy with graphene (or hBN) are contrary to the theory assumptions. Secondly, the RA product in our experiments is 5 orders of magnitude greater than the theoretical value, $< 0.003 \Omega \mu\text{m}^2$, obtained for ‘K-point filtering’ and attributed to hybridization and covalent bonding [10]. Therefore, we draw attention to two features specific to the FM/graphene interface which have not been considered previously in the context of MTJs: doping due to contact with a metal [34,35] and exchange splitting due to proximity to a ferromagnet that gives rise to a difference in the density of states (DoS) between spin-up and spin-down carriers in graphene [5-7]. Triggered by annealing, graphene conforms to corrugated surfaces of polycrystalline FMs, and for $N>1$ this would cause delamination of a van der Waals-bonded few-layer crystal into two loosely coupled thinner graphenes. Subsequently, these two separately doped and exchange proximitised graphene layers become spin-polarised electrodes defining the device behavior, with a relatively small value of MR but qualitatively new features.

In this situation, unique to graphene, the spin polarization of majority/minority charge carriers should depend on the sign and level of doping (even for the same exchange splitting). This is because for spin-split bands in gapless graphene the type (p- or n-) of doping would determine which spin components (up- or down-) would have larger DoS at the Fermi level, as illustrated schematically in Fig. 2c. To evaluate the doping in our devices, we prepared test samples as described in Supplementary Note 4 and measured gate-dependent charge transport in the vicinity of Co and Py contacts. This showed that graphene in contact with Co is n-doped and graphene in contact with Py is p-doped, with corresponding shifts of the Fermi energy, E_F , from the charge neutrality point ≈ -100 meV and $+200$ meV, respectively (Supplementary Note 4). A scenario corresponding to such doping is illustrated in Fig. 2c for the charge transfer and proximitised exchange splitting generated by the spin-dependent DoS of Co, Py (drawn schematically with partly occupied 3d and 4s states) and the few-layer graphene spacer. Here the exchange energy in graphene is assumed to be much smaller than ~ 100 meV shift of E_F due to doping, in accordance with the recent estimate $\sim \mu_B \times |\mathbf{B}_{\text{exch}}| \sim 50 \mu\text{eV}$ [6] for induced spin polarization in graphene on YIG. In this simple picture, at E_F spin-

up electrons represent the majority in n-doped graphene and spin-down electrons are the majority in p-doped graphene. It follows directly that the sign of MR will be negative. Furthermore, the magnitude of MR should be small due to a small value of exchange spin splitting. Note that the proposed interpretation also explains why, upon annealing, MR increases for $N = 1$ but decreases and changes sign for $N \geq 2$. A monolayer graphene can conform only to one of the FM layers and the increase in MR can be explained by an improved contact on one side, while few-layer films can split to conform to the ferromagnetic grains on both sides [33], resulting in negative MR as described above.

To further verify the proposed model, we investigated the bias dependence of MR in devices with $N=2$ and 3 both before and after annealing. For this system (in contrast to standard MTJs), the role of increasing bias, V_b , is not only to shift the chemical potentials on the two sides of the barrier but also to change graphene doping (as shown schematically in Fig. 4), like in a graphene-based vertical transistor [23]. Due to the large quantum capacitance in such systems [23], graphene doping can substantially change and even reverse the sign, leading to a change of sign of MR. This is exactly what we observe in few-layer graphene devices, exemplified by the measurements shown in Fig. 4 for trilayer graphene: a change of MR sign from negative to positive for $V_b > +100$ mV (electrons flow from Py to Co), and notable asymmetry in the rate of MR decrease for positive and negative V_b . Note that to change the Fermi level in the Co electrode sufficiently to lead to the MR sign reversal would require $V_b \sim 800$ meV, as shown for Co/SrTiO₃/La_{0.7}Sr_{0.3}MnO₃ MTJs [36]. In our case, we were able to tune the MR using much smaller bias voltages: from MR = -0.6% at $V_b = 0$ to +0.2% at $V_b = +230$ mV, with the sign change at $V_b \approx +100$ mV and from -0.6% to zero at $V_b = -250$ mV. Remarkably, the V_b value corresponding to the change of sign of MR agrees with the doping-induced shift of E_F in graphene adjacent to Co (see Supplementary Note 4).

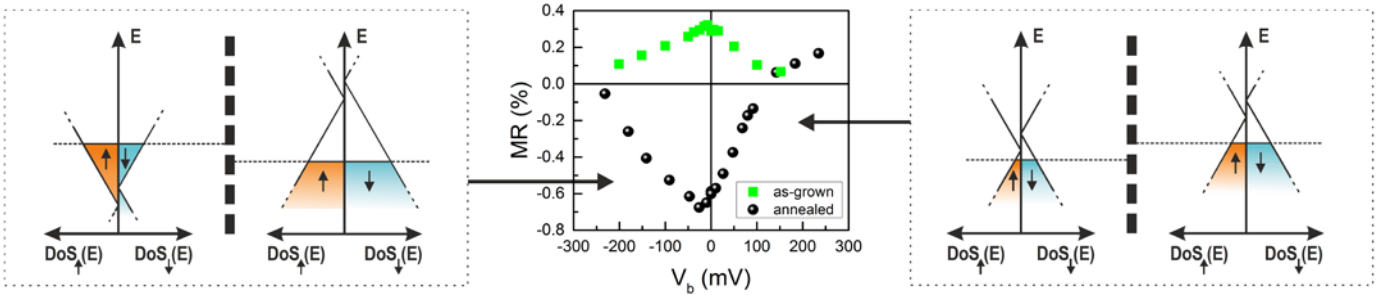


FIG. 4: Bias dependence of the magnetoresistance before and after annealing. Central panel: Experimental dependence of MR on the bias voltage, V_b , for a trilayer graphene device before (■) and after (●) annealing. For the annealed device, MR changes sign from negative to positive at $V_b \approx +120$ mV (corresponding to carriers flowing from Py to Co). **Right panel:** Schematic DoS in the two doped and proximitised graphene ‘electrodes’ at maximum positive V_b (see text). As E_F of graphene adjacent to Co shifts into the valence band at $V_b > +120$ mV, spin-down carriers have a higher DoS in both graphene ‘electrodes’ and MR becomes positive (c.f. Fig. 2c). **Left panel:** Schematic DoS in the two graphene ‘electrodes’ at maximum negative V_b . No sign change of MR is expected, in agreement with experiment, as negative V_b does not change the prevalent spin type at E_F for the two graphene electrodes.

In conclusion, our results reveal a new role played by graphene in MTJs. In place of the earlier discussed ‘K-point spin filtering’ suggested for both FM-graphene-FM and FM-hBN-FM epitaxial-quality interfaces [9,10], we find that the major role is played by a combined effect of metal-induced doping and exchange-proximity induced spin polarization in graphene. This mechanism points towards a possible use of proximitised graphene in devices where magnetoresistance can be controlled by the size and polarity of charge transfer, somewhat similar to the bias-dependent MR governed by the spin polarization at the interface between Co and an organic semiconductor [37]. More ambitiously, if a larger exchange splitting in graphene can be achieved by proximity to a ferromagnetic insulator, as predicted by theory [7,8], one may achieve *electrostatic* control over MR by implementing G-hBN-G in van der Waals heterostructures. In this case the TMR effect would be enhanced or suppressed by varying a bias voltage in FM-G-hBN-G-FM’ junctions with mono- or bilayer hBN in the middle. Potentially, this can drive proximitised graphene into the half-metallic state at optimal doping, offering exciting prospects for graphene in magnetic devices.

METHODS

All devices were made using a 4-step fabrication process shown schematically in Supplementary Fig. S1. To produce an aperture in the double-sided $\text{SiN}_x(100 \text{ nm})/\text{Si}(200 \text{ }\mu\text{m})/\text{SiN}_x(100 \text{ nm})$ wafer used as support for FM/graphene(hBN)/FM’ structures, we first used plasma etching (Oxford PlasmaLab System 100 ICP) with a Shipley 1813 photoresist etch mask to remove a $\sim 300 \times 300 \text{ }\mu\text{m}$ area of SiN_x . This was followed by wet etching of the exposed Si in a KOH solution (30 wt. % in H_2O at $90 \text{ }^\circ\text{C}$) until a 100 nm thick SiN_x window was produced, with a typical area $\sim 25 \text{ }\mu\text{m} \times 25 \text{ }\mu\text{m}$. After that a 3.5 μm diameter circular aperture was drilled in the SiN_x window using a dual-beam FEI Nova NanoLab 600 focused ion beam (FIB) with 30 kV Ga^+ ions at a current of 0.1 nA (prior alignment was done with the SEM column to minimize damage). By approaching the SiN_x membrane from the bottom side (Supplementary Fig. S1) FIB etching produced a concave profile of the aperture walls, ensuring that the thin metal film deposited in the next step was continuous, minimizing any complications due to e.g. fracture. In the second step, a few-layer graphene (or hBN) flake was mechanically exfoliated onto a PMMA membrane. The number of layers, N , was estimated from optical contrast and later confirmed using Raman spectroscopy. The flake was then transferred onto the aperture using a dry transfer method [19,30]. To ensure good adhesion between graphene (or hBN) and SiN_x , we selected flakes much larger than the aperture (minimum area of $\sim 100 \text{ }\mu\text{m}^2$). In addition, the wafer was heated to 60°C during the transfer, which was followed by a 45-second annealing at 130°C . The PMMA was then detached from the flakes by gently dipping the sample in acetone (10 min) and the residual solvent was removed in isopropyl alcohol and hexane baths. The suspended flake was characterized by differential interference contrast (DIC) microscopy, atomic force microscopy (AFM) and Raman spectroscopy – information about the number of atomic layers was extracted from Raman spectra (for graphene) or AFM data (for hBN). In the third step, $\text{Co}(20 \text{ nm})/\text{Ti}(6 \text{ nm})/\text{Au}(50 \text{ nm})$ were deposited onto graphene(hBN)/ SiN_x through an Al shadow mask in an e-beam evaporator (Leybold L560 Universal Coating System) at a base vacuum of 10^{-6} mbar and a low deposition

rate (0.03 nm/s) to reduce stresses. In the final fourth step, we evaporated Ni_{0.8}Fe_{0.2}(20 nm)/Ti(6 nm)/Au(120 nm) on the bottom side using the same conditions as for the top side deposition.

To image and characterize the samples at various fabrication steps we used optical, atomic force (AFM), scanning electron (SEM) and Raman microscopies. AFM imaging was done in air using a Bruker Dimension FastScan in PeakForce Tapping mode and ScanAsyst-Fluid+ tips at a 0.3 $\mu\text{m}\cdot\text{s}^{-1}$ scan rate and 1 nN peak tapping force. For SEM imaging and Raman spectroscopy, a Zeiss Ultra Plus SEM and a Renishaw inVia Raman Microscope (laser excitation at 532 nm, laser spot power at sample area 0.17 mW) were used. SEM imaging was done only for test samples and never the devices, as the electron beam is known to introduce surface contamination. Device characterization is discussed in detail in Supplementary Note 2.

REFERENCES

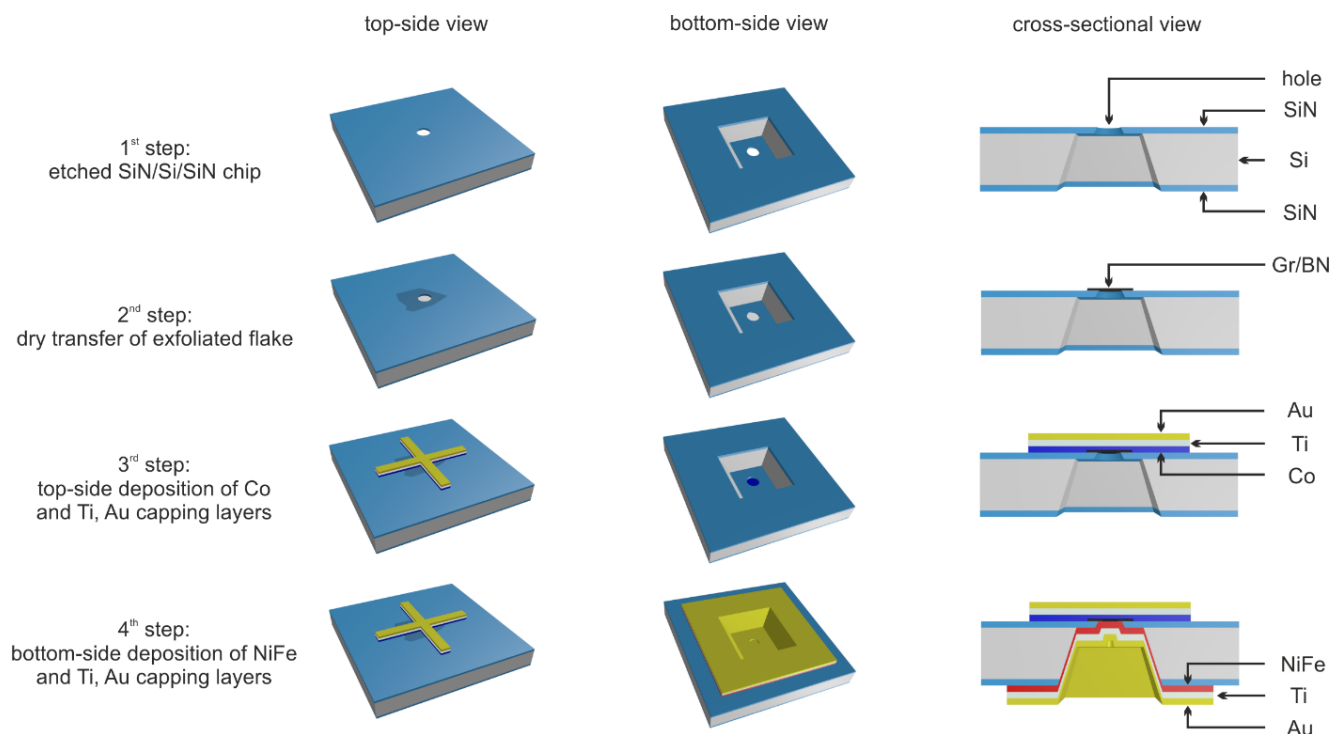
- [1] Roche, S. *et al.* Graphene spintronics: the European Flagship perspective. *2D Mater.* **2**, 030202 (2015).
- [2] Tombros, N., Jozsa, C., Popinciuc, M., Jonkman, H. T. & van Wees, B. J. Electronic spin transport and spin precession in single graphene layers at room temperature. *Nature* **448**, 571-574 (2007).
- [3] Han, W., Kawakami, R. K., Gmitra, M. & Fabian, J. Graphene spintronics. *Nature Nanotech.* **9**, 794-807 (2014).
- [4] Nair, R. R. *et al.* Spin-half paramagnetism in graphene induced by point defects. *Nature Phys.* **8**, 199-202 (2012).
- [5] Wang, Z., Tang, C., Sachs, R., Barlas, Y. & Shi, J. Proximity-induced ferromagnetism in graphene revealed by the anomalous Hall effect. *Phys. Rev. Lett.* **114**, 016603 (2015).
- [6] Leutenantsmeyer, J. C., Kaverzin, A. A., Wojtaszek, M. & van Wees, B. J. Proximity induced room-temperature ferromagnetism in graphene probed with spin currents. *Preprint at arXiv:1601.00995*.
- [7] Yang, H. X. *et al.* Proximity effects induced in graphene by magnetic insulators: first-principles calculations on spin filtering and exchange-splitting gaps. *Phys. Rev. Lett.* **110**, 046603 (2013).
- [8] Wei, P. *et al.* Strong interfacial exchange field in the graphene/EuS heterostructure. *Nature Mater.* - Advance Online Publication (2016); DOI: 10.1038/NMAT4603.
- [9] Karpan, V. M. *et al.* Graphite and graphene as perfect spin filters. *Phys. Rev. Lett.* **99**, 176602 (2007).
- [10] Yazyev, O. V. & Pasquarello, A. Magnetoresistive junctions based on epitaxial graphene and hexagonal boron nitride. *Phys. Rev. B* **80**, 035408 (2009).
- [11] Dlubak, B. *et al.* Graphene-passivated nickel as an oxidation-resistant electrode for spintronics. *ACS Nano* **6**, 10930-10934 (2012).
- [12] M. B. Martin *et al.* Sub-nanometer atomic layer deposition for spintronics in magnetic tunnel junctions based on graphene spin-filtering membranes. *ACS Nano* **8**, 7890-7895 (2014).
- [13] M. B. Martin *et al.* Protecting nickel with graphene spin-filtering membranes: A single layer is enough. *Appl. Phys. Lett.* **107**, 012408 (2015).

- [14] Li, W., Xue, L., Abruña, H. D. & Ralph, D. C. Magnetic tunnel junctions with single-layer-graphene tunnel barriers. *Phys. Rev. B* **89**, 184418 (2014).
- [15] Park, J.-H. & Lee, H.-J. Out-of-plane magnetoresistance in ferromagnet/graphene/ferromagnet spin-valve junctions. *Phys. Rev. B* **89**, 165417 (2014).
- [16] Cobas, E., Friedman, A. L., van't Erve, O. M. J., Robinson, J. T. & Jonker, B. T. Graphene as a tunnel barrier: graphene-based magnetic tunnel junctions. *Nano Lett.* **12**, 3000-3004 (2012).
- [17] Chen, J.-J. et al. Layer-by-layer assembly of vertically conducting graphene devices. *Nature Commun.* **4**, 1921 (2013).
- [18] Meng, J., Chen, J.-J., Yan, Y., Yu, D.-P. & Liao, Z.-M. Vertical graphene spin valve with Ohmic contacts. *Nanoscale* **5**, 8894-8898 (2013).
- [19] Iqbal, M. Z. et al. Spin valve effect of NiFe/graphene/NiFe junctions. *Nano Res.* **6**, 373-380 (2013).
- [20] Geim, A. K. & Grigorieva, I. V. Van der Waals heterostructures. *Nature* **499**, 419-425 (2013).
- [21] Kretinin, A. V. et al. Electronic properties of graphene encapsulated with different two-dimensional atomic crystals. *Nano Lett.* **14**, 3270-3276 (2014).
- [22] Bunch, J. S. et al. Impermeable atomic membranes from graphene sheets. *Nano Lett.* **8**, 2458-2462 (2008).
- [23] Britnell, L. et al. Field-effect tunneling transistor based on vertical graphene heterostructures. *Science* **335**, 947-950 (2012).
- [24] Kamalakar, M. V., Dankert, A., Bergsten, J., Ive, T. & Dash, S. P. Enhanced tunnel spin injection into graphene using chemical vapor deposited hexagonal boron nitride. *Sci. Rep.* **4**, 6146 (2014).
- [25] Piquemal-Banci, M. et al. Magnetic tunnel junctions with monolayer hexagonal boron nitride tunnel barriers. *Appl. Phys. Lett.* **108**, 102404 (2016).
- [26] Tsymbal, E. Y., Mryasov, O. N. & LeClair, P. R. Spin-dependent tunnelling in magnetic tunnel junctions. *J. Phys. Condens. Matter* **15**, R109-R142 (2003).
- [27] Dankert, A., Kamalakar, M. V., Wajid, A., Patel, R. S. & Dash, S. P. Tunnel magnetoresistance with atomically thin two-dimensional hexagonal boron nitride barriers. *Nano Res.* **8**, 1357-1364 (2015).
- [28] Shang, C. H., Nowak, J., Jansen, R. & Moodera, J. S. Temperature dependence of magnetoresistance and surface magnetization in ferromagnetic tunnel junctions. *Phys. Rev. B* **58**, R2917-R2920 (1998).
- [29] Jansen, R. & Moodera, J. S. Magnetoresistance in doped magnetic tunnel junctions: effect of spin scattering and impurity-assisted transport. *Phys. Rev. B* **61**, 9047-9050 (2000).
- [30] Britnell, L. et al. Electron tunneling through ultrathin boron nitride crystalline barriers. *Nano Lett.* **12**, 1707-1710 (2012).
- [31] Kästle, G., Boyen, H.-G., Schröder, A., Plettl, A. & Ziemann, P. Size effect of the resistivity of thin epitaxial gold films. *Phys. Rev. B* **70**, 165414 (2004).
- [32] Mayorov, A. S. et al. Micrometer-scale ballistic transport in encapsulated graphene at room temperature. *Nano Lett.* **11**, 2396-2399 (2011).

- [33] Cullen, W. G. *et al.* High-fidelity conformation of graphene to SiO₂ topographic features. *Phys. Rev. Lett.* **105**, 215504 (2010).
- [34] Nouchi, R., Saito, T. & Tanigaki, K. Determination of carrier type doped from metal contacts to graphene by channel-length-dependent shift of charge neutrality points. *Appl. Phys. Express* **4**, 035101 (2011).
- [35] Giovannetti, G. *et al.* Doping graphene with metal contacts. *Phys. Rev. Lett.* **101**, 026803 (2008).
- [36] De Teresa, J. M. *et al.* Inverse tunnel magnetoresistance in Co/SrTiO₃/La_{0.7}Sr_{0.3}MnO₃: new ideas on spin-polarized tunneling. *Phys. Rev. Lett.* **82**, 4288-4291 (1999).
- [37] Barraud C. *et al.* Unravelling the role of the interface for spin injection into organic semiconductors. *Nature Phys.* **6**, 615-620 (2010).

Supplementary Information

Supplementary Note 1. Device fabrication.

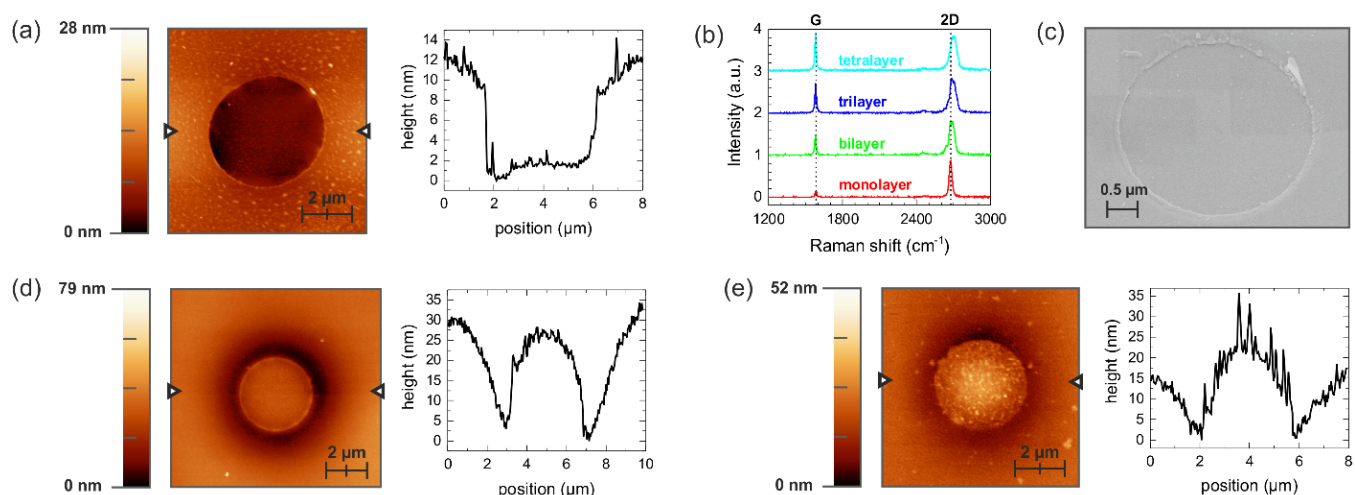


Supplementary Figure S1. Schematics of device fabrication. Details of each fabrication step are given in Methods.

Compared to earlier experimental studies of vertical FM-graphene-FM devices that used FM deposition directly onto graphene (either suspended [S1] or exfoliated onto a polymer membrane [S2]), we used fewer fabrication steps, avoided using more aggressive solvents, such as NMP, and used thinner ferromagnetic films, thereby reducing stresses in the devices. Furthermore, FIB etching from the back side of the device made it possible to achieve an aperture profile that ensured that both FM films (Co and Py) were continuous across the aperture. This, together with the relatively large aperture sizes ensured a clear switching behavior of the FM films, therefore avoiding complications due to e.g. magnetic domain configurations. The device geometry and dimensions were the same in all our samples and only the number of graphene layers was varied. This allowed us to unambiguously relate the measured magnetoresistance to the properties of the graphene barrier.

Supplementary Note 2. Device characterization.

To characterize our samples at different stages of fabrication we used optical, atomic force (AFM), scanning electron (SEM) and Raman microscopies. To assess the roughness and quality of graphene spacers, suspended areas of the devices were imaged using AFM. This showed that the surface of the suspended graphene was clean and very smooth, without any signs of polymer residue. The RMS roughness for a typical graphene monolayer was 0.47 nm (Supplementary Fig. S2a). We note that this is an important improvement compared to the earlier report [S2] where a similar fabrication method was used but required treatment with NMP-based solvents. As a test, we have prepared several samples using a PMMA-based transfer technique followed by the removal of resist with NMP. This resulted in much dirtier surfaces, typically showing residue with oil-like adhesion and viscosity.



Supplementary Figure S2. Characterization of our devices at different steps of fabrication. (a) AFM image of a suspended monolayer graphene flake before the deposition of metal electrodes (step 2 in Supplementary Fig. S1). The size of the flake is much larger than the aperture area. A height profile corresponding to the cross section indicated by the triangles is shown on the right. Graphene sags and partially adheres to the sides of the aperture as is common for suspended atomically thin crystals. (b) Raman spectra of suspended mono-, bi-, tri- and tetralayer graphene. The D peak is absent indicating high quality of graphene spacers in all our devices. (c) Scanning electron microscope (SEM) image of a finished bilayer hBN device taken from the bottom side after the deposition of both FM films (step 4 in Supplementary Fig. S1). The bottom FM film (Py) is continuous across the step between the ring-shaped indentation (corresponding to the thickness of the supporting SiN_x membrane) and outer areas, ensuring good electrical contact. The image was taken under 30° tilt. (d) AFM image of a suspended bilayer graphene after metal deposition on both sides (step 4 in Supplementary Fig. S1). A height profile corresponding to the cross section indicated by the triangles is shown on the right. Sagging (bending) of the supporting SiN_x membrane under the weight of the top FM film (Co) and of graphene under the weight of the thicker bottom FM (Py) are clearly seen. (e) Same as (d) but for a bilayer hBN device. Both devices have a junction area of $\approx 11 \mu\text{m}^2$.

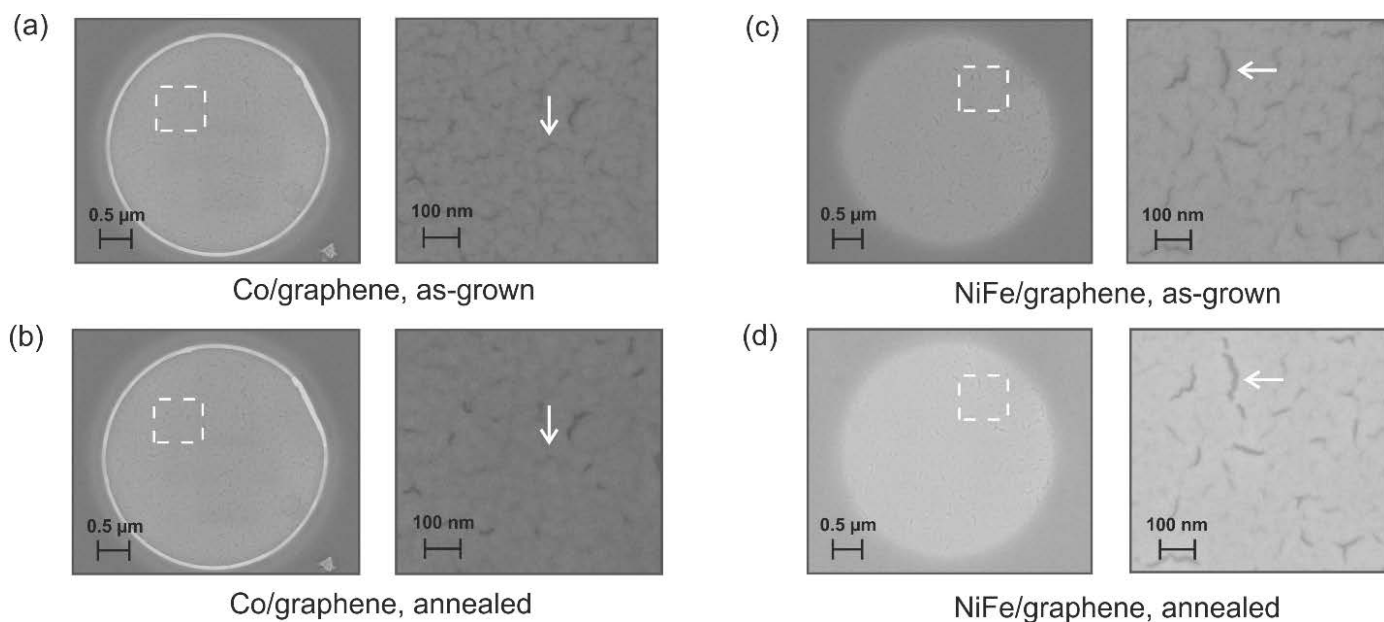
To verify the number of graphene layers in the transferred exfoliated graphene, we used Raman spectroscopy. Typical spectra for suspended mono-, bi-, tri- and tetralayer graphene are shown in Supplementary Fig. S2b. The

high quality of our graphene membranes was confirmed by Raman maps acquired with a resolution of 0.7 μm , revealing the absence of the D peak everywhere in the suspended areas.

The AFM image of a typical graphene device after the deposition of both FM electrodes is shown in Supplementary Fig. S2d. The corresponding cross-sectional profile shows a smooth surface and a ‘Mexican hat’ shape typical for all our devices. This shape results from bulging in the graphene area under the weight of the relatively thick (146 nm) metal film and bending of the SiN window around the aperture under the weight of a thinner (76 nm) metal film. The AFM image of the finished bilayer hBN device in Supplementary Fig. S2e shows a rougher surface, probably due to island formation during Co growth on hBN as reported earlier [S3]. Importantly, the more irregular growth of Co on hBN did not affect the performance of our devices as both the Co layer and the capping Ti/Au layers are much thicker than the average roughness.

To characterize the effect of annealing on the microstructure of the FM layers at the FM/graphene interface, we fabricated test devices with monolayer graphene where only one FM layer (either Co or Py) was deposited on the top side of the suspended graphene (Supplementary Fig. S3). All process parameters used for FM deposition in these test devices and subsequent annealing were exactly the same as for the devices used to study the magnetoresistance, to ensure comparable characteristics of the FM films. As graphene is effectively transparent to the electron beam, it was possible to see the graphene/FM interface, including the shapes of individual grains in our polycrystalline films and the boundaries between them. Comparison of the SEM images before and after annealing revealed clear signs of rearrangements of the crystallites after annealing. For example, some of the ‘cracks’ between NiFe grains that were visible on the as-grown samples became wider after annealing, indicating relaxation of strains as discussed in the main text (Supplementary Fig. S3c,d). For Co films, fewer and less defined ‘cracks’ are seen after annealing, indicating a smoother, less corrugated surface. At the same time, there was no increase in the size of the crystallites, as could be expected if re-crystallization had taken place. We note that SEM imaging was only used for the above test devices and never for the devices used for transport measurements, as SEM imaging is known to induce surface contamination.

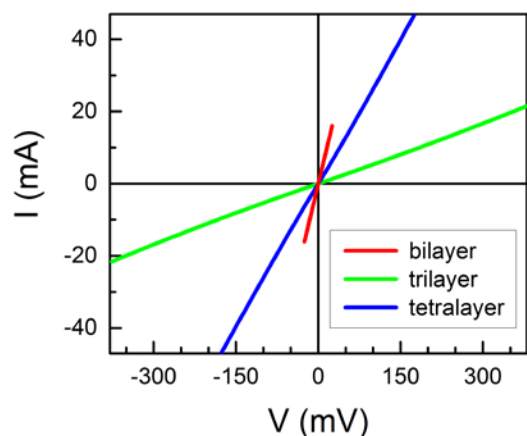
To investigate the mechanical strength of the bonding between graphene and the FM films, we prepared several samples consisting of graphene mechanically exfoliated onto Si/SiO_x substrate and covered by thin Co/Ti/Au or NiFe/Ti/Au films. The films were of the same thicknesses and evaporated under the same conditions as those used for our TMR devices. Then the FM films were peeled off the substrate using a strongly adhesive tape to see which interfaces have the weakest adhesion. In all cases, the Au/Ti/FM/graphene stack completely came off of the substrate, leaving the bare SiO_x surface. A similar behavior was found for few-layer graphene/FM stacks. This demonstrated a very strong adhesion between graphene and the FM films, stronger even than the adhesion between graphene and SiO_x [S4], supporting our expectation that graphene layers adjacent to the polycrystalline FM films conform to the corrugated surfaces of the latter.



Supplementary Figure S3. SEM imaging of Co and NiFe films through graphene, before and after annealing. All images were taken from the bottom side of the device. Graphene is effectively transparent to the electron beam, which allows a detailed view of the structure of the ferromagnetic films. **(a,c)** SEM images of Co and NiFe films, respectively, taken before annealing (as-grown). The thickness of both Co or NiFe was 20 nm, followed by capping layers of Ti(6 nm)/Au(50 nm). **(b,d)** SEM images of the same Co and NiFe films as in (a,c) after annealing in Ar/H₂ atmosphere at 300°C for 3h. The areas marked by dashed lines on the left images of each panel are shown at higher magnification on the right. Arrows indicate areas where changes due to annealing are clearly seen, such as ‘cracks’ between individual grains in our polycrystalline films.

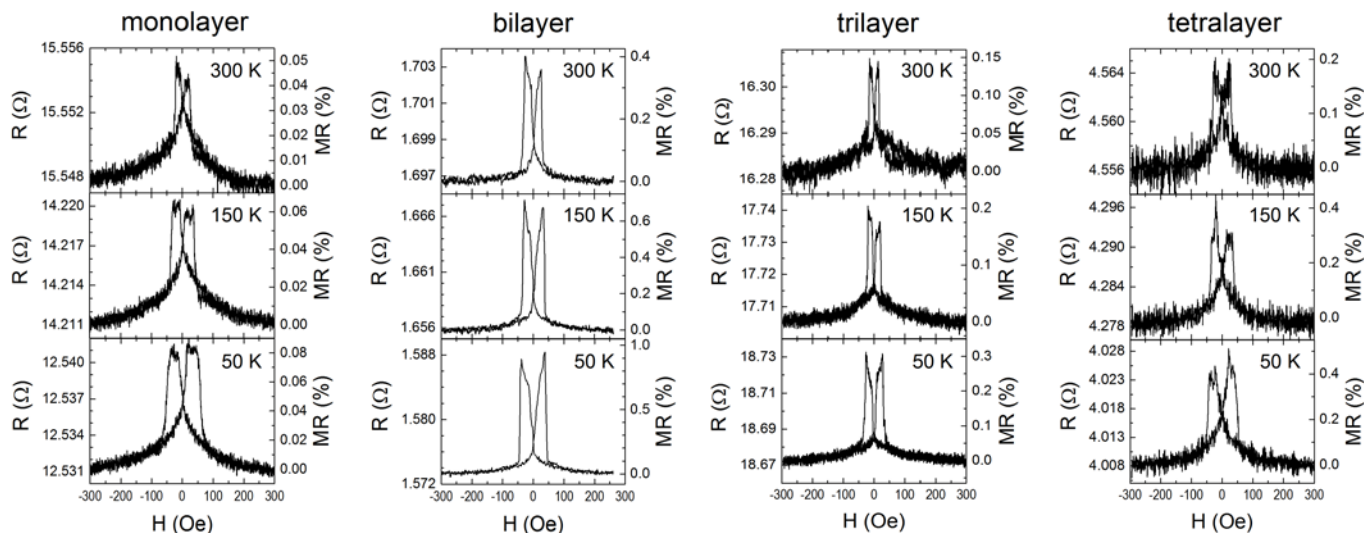
Supplementary Note 3. Magnetotransport measurements and *I-V* characteristics.

All FM-graphene-FM’ devices exhibited linear current-voltage characteristics over a large voltage range, irrespective of the number of layers (Supplementary Fig. S4). *I-V* characteristics were linear both before and after annealing.

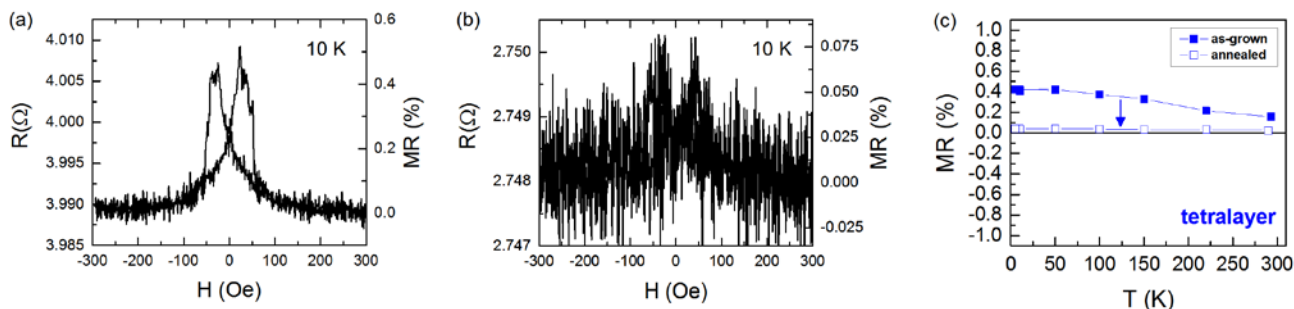


Supplementary Figure S4. *I-V* characteristics of FM-graphene-FM’ devices. Shown are typical *I-V* characteristics of ‘as-grown’ devices (before annealing) with bi- (—), tri- (—) and tetralayer (—) graphene separating the FM films. All data acquired at 10 K.

Magnetotransport properties of the tetralayer ($N = 4$) graphene device after annealing are qualitatively similar to the behavior seen for the devices with $N= 2$ and 3 (see main text). Following annealing, the MR dropped from 0.43% to 0.06%, similar to bi- and trilayer devices, but did not lead to a full reversal of the MR sign (Supplementary Fig. S6). We speculate that the reason for this difference can be in less effective conformation and strain relaxation at the interfaces between the FM films and the tetralayer graphene: The latter is less flexible and cannot conform to the corrugated FM film as well as the thinner bi- or trilayer, possibly resulting in smaller spin polarizations in graphene layers adjacent to the FMs or different levels of doping.



Supplementary Figure S5. Magnetoresistance of as-grown graphene devices at higher temperatures. Shown is the magnetic field dependent resistance, $R(H)$, for mono-, bi-, tri- and tetralayer graphene devices. The behavior is typical for vertical TMR devices (see main text). The coercivity of the Co layer increases monotonically with decreasing temperature leading to more clearly separated switching of Co and NiFe and broader MR features.



Supplementary Figure S6: Magnetoresistance of a tetralayer graphene device. (a,b) Low-temperature magnetoresistance sweeps before and after annealing, respectively. (c) Temperature-dependent MR before (■) and after (□) annealing; the arrow indicates the MR change due to annealing.

Supplementary Note 4. Metal-induced doping of graphene.

To determine the level of doping of graphene from the adjacent FM films in our devices, we prepared specially designed test samples and measured gate-dependent charge transport in the vicinity of Co and Py contacts, a technique similar to that used in ref. [S5]. To this end, a rectangular graphene flake was mechanically exfoliated onto a Si/SiO_x(290 nm) substrate. Co and NiFe bars were then evaporated on top of graphene at different spacings, $s = 0.5 \mu\text{m}$ to $4 \mu\text{m}$, as shown in Supplementary Fig. S7d. To ensure compatibility with magnetotransport measurements in our FM-graphene-FM' devices, we used identical deposition conditions for the FM films. For each Co or NiFe contact pair separated by a spacing s we measured the resistance, R , of the graphene channel as a function of gate voltage, V_g . For small s , doping from the FM contacts is expected to dominate the measured $R(V_g)$, whereas for larger s the resistance will be largely determined by environmental doping (substrate and adsorbate induced). We therefore expect two Dirac points to emerge in $R(V_g)$, one originating from the metal-induced doping that is at a maximum directly under the contacts but also extends to a $\sim 100\text{-}300 \text{ nm}$ distance into the graphene channel (the exact distance depending on the metal) [S6-S9], and another one from the central area of the graphene channel. Accordingly, we designate the gate-dependent resistance of the contact-doped part of the channel and of its central region as $R_{\text{metal}}(V_g)$ and $R_{\text{envr}}(V_g)$, respectively. From the Dirac point associated with $R_{\text{metal}}(V_g)$, it is then possible to extract the shift of the Fermi level, E_F , due to doping from the ferromagnetic films.

Transport measurements were done in a quasi-4-terminal geometry as shown in Supplementary Fig. S7c. In the case of Co contacts, for the largest spacing $s = 4 \mu\text{m}$ we found a single peak in $R(V_g)$ with the Dirac point at $V_g = +11 \text{ V}$ (Supplementary Fig. S7a), i.e., away from the metal graphene is p-doped as is usual for environmental doping of graphene on SiO_x. For $s = 3 \mu\text{m}$ and below, a second peak developed at negative V_g , which became most apparent for $s = 0.5 \mu\text{m}$ and $1 \mu\text{m}$. This second Dirac point, corresponding to electron doping, is due to a large part of the graphene channel being doped by the Co contacts and its resistance becoming an increasingly large part of the total R . To extract the carrier density associated with doping by Co contacts, we used a two-peak fitting procedure based on a phenomenological model proposed in ref. [S10]. In this model, the total carrier density for each peak is given by

$$n_{\text{tot}} = [n_0^2 + n(V_g)^2]^{1/2}, \quad (1)$$

where n_0 is the intrinsic carrier density and n the carrier density induced by the gate voltage V_g according to $n(V_g) = (C/e)(V_g - V_0)$, where V_0 is the gate voltage corresponding to the Dirac point and C the capacitance of the SiO_x dielectric layer. The total resistance $R_{\text{tot}}(V_g) = R_C + R_{\text{metal}}(V_g) + R_{\text{envr}}(V_g)$ then results from the sum of the constant contact resistance R_C and the resistance of the two differently doped graphene areas, $R_{\text{metal}}(V_g) \propto (n_{\text{metal}}e\mu)^{-1}$ and $R_{\text{envr}}(V_g) \propto (n_{\text{envr}}e\mu)^{-1}$, where n_{metal} and n_{envr} are determined by eq. (1). The positions, V_0 , of the two Dirac points extracted from the fits for different s are shown in Supplementary Fig. S7c. The fact that both Dirac points remain at approximately the same respective V_g for all s confirms the validity of our approach.

To relate n_{metal} and the associated shift in E_F due to doping we can use [S11]

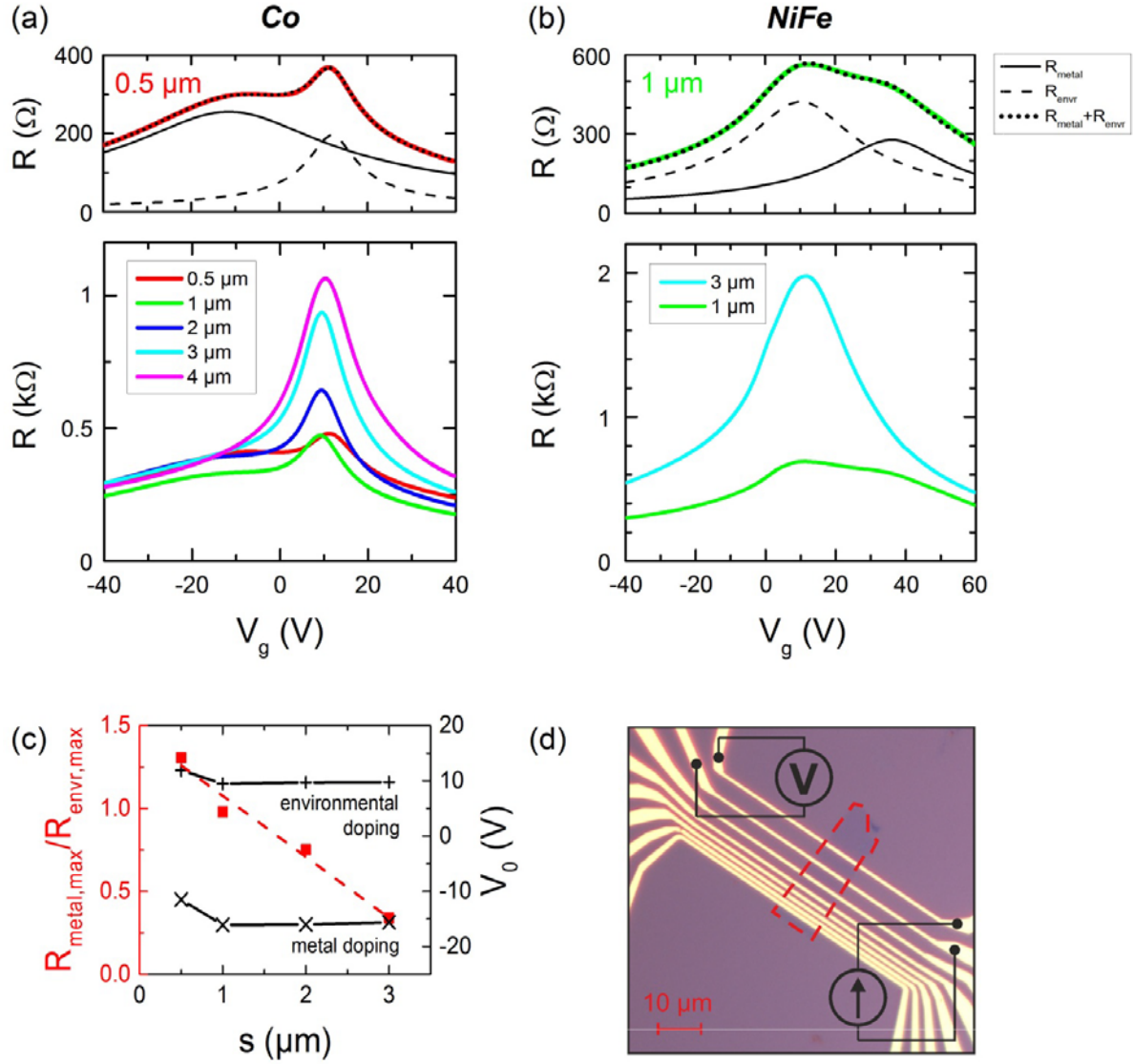
$$n(E_F) = \frac{E_F^2}{(\hbar v_F)^2} . \quad (2)$$

On the other hand, the gate-induced carrier density, $n(V_g)$, can be found as

$$n(V_g) = \frac{V_g \epsilon_0 \epsilon_r}{d \cdot e} , \quad (3)$$

where $v_F \sim 10^8$ cm/s is graphene's Fermi velocity, e the electron charge, ϵ_0 the permittivity of the free space and $\epsilon_r = 3.9$ and $d = 290$ nm the permittivity and thickness of the SiO_x layer, respectively. Using (2), (3) and $V_0 \approx -11$ V for the Dirac point associated with doping from the Co contacts, we find doping-induced $E_F \approx -105$ meV, i.e. graphene is n-doped.

A similar analysis for the sample with NiFe contacts showed that graphene in contact with NiFe is p-doped, with a larger Fermi level shift compared to Co, $E_F \approx +190$ meV. In this case, a single $R(V_g)$ peak at $V_0 \approx +10$ V is found for $s = 3$ μm and a second peak at $V_0 \approx +36$ V develops at smaller s , corresponding to $E_F \approx +190$ meV (Supplementary Figure S7b).



Supplementary Figure S7: Doping of graphene by Co and NiFe. (a, b) Resistance R as a function of gate voltage, V_g , for graphene devices with Co and NiFe contacts, respectively. Bottom panels show measured $R(V_g)$ for different contact separations, s . Top panels show the results of the two-peak fitting procedure described in the text for the smallest contact separations, $s = 0.5 \mu\text{m}$ and $s = 1 \mu\text{m}$ for Co and NiFe, respectively. Individual peaks for $R_{\text{metal}}(V_g)$ and $R_{\text{envr}}(V_g)$ are shown by solid and dashed lines, respectively. The dotted lines show the sum of the two peaks, in agreement with the measured $R(V_g)$ shown by the solid red line. The constant contact resistance, R_C , obtained from the fits has been subtracted for clarity. (c) Positions, V_0 , of the two Dirac points for the device with Co contacts as a function of the contact spacing, s (crosses). Filled red symbols show the corresponding ratios of the maximum resistances of the two peaks. As expected, the resistance corresponding to metal doping, $R_{\text{metal,max}}$, becomes dominant at the smallest s . (d) Optical image of the device with Co contacts and the measurement geometry. Graphene is outlined by the dashed red line.

Supplementary references

- S1. Li, W., Xue, L., Abruña, H. D. & Ralph, D. C. Magnetic tunnel junctions with single-layer-graphene tunnel barriers. *Phys. Rev. B* **89**, 184418 (2014).
- S2. Park, J. H. & Lee, H. J. Out-of-plane magnetoresistance in ferromagnet/graphene/ferromagnet spinvalve junctions. *Phys. Rev. B* **89**, 165417 (2014).
- S3. Auwärter, W., Muntwiler, M., Greber, T. & Osterwalder, J. Co on h-BN/Ni(111): from island to island-chain formation and Co intercalation. *Surf. Sci.* **511**, 379-386 (2002).
- S4. Koenig S. P., Boddeti, G., Dunn, M. L. & Bunch, S. Ultrastrong adhesion of graphene membranes. *Nature Nanotech.* **6**, 543-546 (2011).
- S5. Nouchi, R., Saito, T. & Tanigaki, K. Determination of carrier type doped from metal contacts to graphene by channel-length-dependent shift of charge neutrality points. *Appl. Phys. Express* **4**, 035101 (2011).
- S6. Lee, E. J. H., Balasubramanian, K., Weitz, R. T., Burghard, M. & Kern, K. Contact and edge effects in graphene devices. *Nature Nanotech.* **3**, 486 - 490 (2008).
- S7. Blake, P. et al. Influence of metal contacts and charge inhomogeneity on transport properties of graphene near the neutrality point. *Solid State Commun.* **149**, 1068–1071 (2009).
- S8. Ben Shalom, M. et al. Quantum oscillations of the critical current and high-field superconducting proximity in ballistic graphene. *Nature Phys.* **12**, 318–322 (2016).
- S9. Allen, M. T. et al. Visualization of phase-coherent electron interference in a ballistic graphene Josephson junction, *Preprint* at arXiv:1506.06734.
- S10. Kim, S. et al. Realization of a high mobility dual-gated graphene field-effect transistor with Al₂O₃ dielectric. *Appl. Phys. Lett.* **94**, 062107 (2009).
- S11. Das Sarma, S., Adam, S., Hwang, E. H. & Rossi, E. Electronic transport in two-dimensional graphene. *Rev. Mod. Phys.* **83**, 407-470 (2011).